

Numerical study on soot formation in outwardly propagating, iso-octane, rich, cellular flames

Ikeda, Takashi

Department of Mechanical Engineering, Graduate School of Engineering, Kyushu University

Tsuruda, Yoshihiro

Department of Mechanical Engineering, Graduate School of Engineering, Kyushu University

Watanabe, Hiroaki

Department of Advanced Environmental Science and Engineering, Faculty of Engineering Sciences, Kyushu University

Kurose, Ryoichi

Department of Mechanical Engineering and Science, Kyoto University

他

<https://hdl.handle.net/2324/7162479>

出版情報 : Fuel. 305, pp.121520-, 2021-12-01. Elsevier

バージョン :

権利関係 :



Numerical study on soot formation in outwardly propagating, iso-octane, rich, cellular flames

Takashi Ikeda^a, Yoshihiro Tsuruda^a, Hiroaki Watanabe^b, Ryoichi Kurose^c,
Toshiaki Kitagawa^d

^a Department of Mechanical Engineering, Graduate School of Engineering, Kyushu

University, Fukuoka 819-0395, Japan

^b Department of Advanced Environmental Science and Engineering, Faculty of Engineering

Sciences, and International Institute for Carbon-Neutral Energy Research, Kyushu University,

Fukuoka 816-8580, Japan

^c Department of Mechanical Engineering and Science, Kyoto University, Kyoto 615-8540,

Japan

^d Department of Mechanical Engineering, Faculty of Engineering, Kyushu University,

Fukuoka 819-0395, Japan

Abstract

Soot formation in outwardly propagating iso-octane rich unstable cellular flames were investigated by means of a two-dimensional numerical simulation at mixture equivalence ratios of 1.4, 1.6, and 1.8. The formation of a cellular flame structure was observed as an indicator of flame instability. In addition, soot formation was found to be enhanced. The cusp area had a negative flame stretch rate; in contrast, the convex area had a positive flame stretch rate. This difference in stretch rate caused a lower flame front temperature and lower temperature gradient. It was also revealed that a difference in temperature in these areas might affect the soot surface growth, which was dependent on the C_2H_2 concentration in these areas.

Keywords: Soot formation, Direct numerical simulation, Outwardly propagating flame, Iso-octane, Flame instability.

1. Introduction

Lean-burn technology is one of the most effective technologies for improving the thermal efficiency of gasoline engines. It does so by increasing the theoretical cycle efficiency using a high specific heat ratio of air–fuel mixture [1]. In particular, a stratified mixture formed by gasoline direct injection has a greater advantage toward enabling further lean combustion than the lower flammable limit of a homogeneous mixture. In addition, auto-ignition in the end-gas region of the combustion chamber, which causes a serious problem in gasoline engines called knocking, does not occur because no fuel exists in that region [1]. This anti-knock quality enables a higher compression ratio and contributes to a further increase in the thermal efficiency. It is also considered that stratified combustion with gasoline direct injection may yield a more stable operation of the engine with less cycle fluctuation.

While gasoline direct injection stratified combustion has the above advantages, it has a problem of soot emission from a fuel-rich region that is formed undesirably in the mixture [2-5]. Soot formation is driven by complex, nanoscale chemical and physical processes, such as production and consumption of precursor large molecule species, phase changes in nucleation, heterogeneous reactions, and inter-particle collisions. Although many researchers have investigated soot formation over the past few decades [6-9], the underlying physics governing these processes has not been well understood even in a simple flame, not to mention in a flame of stratified combustion or in a flame that expresses instability due to the flame stretch and the thermo-diffusive effects [10]. In particular, for unstable flames, the complexity of soot formation may be

significantly attributed to the complexity of the energy and chemical species transportation through the thermo-diffusive effects. Therefore, in order to understand soot formation in stratified combustion, it is necessary to investigate soot formation during homogeneous combustion with various equivalence ratios, which may then be used to represent each local part in the stratified mixture. The reconstitution of these results may lead to an understanding of soot formation in stratified combustion.

In previous work, one of the authors and his team showed, using a homogeneous mixture, that a luminous flame due to soot emission was observed behind a blue flame in the photograph of a spherically propagating, unstable, iso-octane, rich flame at equivalence ratio of 1.8 [5]. They also indicated that this luminous flame might have formed at the cusp area of the cellular structure of the flame due to flame instability. Flame instability has been studied experimentally, theoretically, and numerically [11-18]. However, there are few fundamental studies on propagating, unstable flames and soot formation from them.

It is important to clarify the mechanism of soot formation from these flames in order to understand the phenomena of soot emission from direct injection, stratified combustion engines. In this study, soot formation in an iso-octane, outwardly propagating, rich, unstable laminar flame was investigated by means of a two-dimensional (2D) numerical simulation with equivalence ratios of 1.4, 1.6 and 1.8. The sine wave was given on the initial flame front as a trigger of the flame instability [19] and the evolution of the cellular structures on the flame front was discussed in terms of the equivalence ratios and their Peclet numbers. In addition, the soot formation characterized by the cellular structure such as the

convex and the cusp areas was also deeply investigated in terms of the interactions of the soot precursor's formation, and the positive and the negative flame stretch rates from the thermo-diffusive effect's point of view.

2. Simulation Methodology

In this study, a 2D numerical simulation of outwardly propagating, iso-octane, premixed laminar flames was performed by an in-house code FK³ [20][21]. The governing equations for the compressible reacting flow are shown below.

$$\frac{\partial \rho}{\partial t} + \frac{\partial \rho u_i}{\partial x_i} = 0, \quad (1)$$

$$\frac{\partial \rho u_i}{\partial t} + \frac{\partial \rho u_i u_j}{\partial x_j} = -\frac{\partial p}{\partial x_i} + \frac{\partial}{\partial x_j} \tau_{ij}, \quad (2)$$

$$\begin{aligned} \frac{\partial \rho h}{\partial t} + \frac{\partial \rho u_i h}{\partial x_i} = \\ \frac{\partial p}{\partial t} + u_i \frac{\partial p}{\partial x_i} + \frac{\partial}{\partial x_i} \left[\rho D_h \left(\frac{\partial h}{\partial x_i} - \sum_k \left(h_k \frac{\partial Y_k}{\partial x_i} \right) \right) - \rho \sum_k (h_k Y_k V_{k,i}) \right] + \tau_{ij} \frac{\partial u_i}{\partial x_i}. \end{aligned} \quad (3)$$

Here, ρ is the mixture gas density, u_i is the gas phase velocity, p is the static pressure, h is the specific total enthalpy, τ_{ij} is the viscous stress tensor, and Y_k is the mass fraction of chemical species k . The radiative heat flux is not considered.

The thermal diffusivity D_h is calculated by

$$D_h = \frac{\lambda_{th}}{\rho C_p}, \quad (4)$$

where λ_{th} is the thermal conductivity, and C_p is the specific heat capacity.

$$\frac{\partial \rho Y_k}{\partial t} + \frac{\partial \rho u_i Y_k}{\partial x_i} = -\frac{\partial}{\partial x_j} (\rho V_{k,i} Y_k) + \rho \dot{\omega}_k. \quad (5)$$

$\dot{\omega}_k$ is the reaction rate of species k . The diffusion velocity of species k in the i direction $V_{k,i}$ is evaluated using the Curtiss–Hirschfelder first-order approximation [22–24].

$$V_{k,i} = -\frac{D_k}{X_k} \nabla X_k, \quad (6)$$

$$D_k = \frac{1 - Y_k}{\sum_{j \neq k} X_j / D_{jk}}. \quad (7)$$

X_j is the species mole fraction of species j , and D_{jk} is the binary diffusion coefficient of species j into species k . The reaction mechanism of iso-octane includes 90 species and 855 elementary reactions, which was simplified using the

Directed Relation Graph with Error Propagation (DRGEP) method with CHEMKIN [30] from the original reaction mechanism updated by Cai and Pitsch, which contained 335 species and 1610 elementary reactions [25] [28]. The simplified mechanism, and the comparison of the burning velocity of the one-dimensional unstretched flames between the original and the simplified mechanism are shown in Supplemental Material. The burning velocity estimated by this simplified mechanism had 5% error compared to that by the original mechanism at equivalence ratio 1.4.

Soot formation is modeled by the following four mechanisms: inception, surface growth, coagulation, and oxidation [6] [26].

$$\left(\frac{dN}{dt}\right)_{Inc.} = c_1 N_A \left(\rho \frac{Y_{C_2H_2}}{W_{C_2H_2}}\right) \exp\left(-\frac{21000}{T}\right), \quad (8)$$

$$\left(\frac{dM}{dt}\right)_{Gro.} = c_2 \left(\rho \frac{Y_{C_2H_2}}{W_{C_2H_2}}\right) \exp\left(-\frac{12100}{T}\right) \left[(\pi N)^{1/3} \left(\frac{6M}{\rho_s}\right)^{2/3}\right], \quad (9)$$

$$\left(\frac{dN}{dt}\right)_{Coa.} = -\left(\frac{24R}{\rho_s N_A}\right)^{1/2} \left(\frac{6}{\pi \rho_s}\right) T^{1/2} M^{1/6} N^{11/6}, \quad (10)$$

$$\left(\frac{dM}{dt}\right)_{Oxi.} = -\left[c_3 \eta \rho \frac{Y_{OH}}{W_{OH}} + c_4 \rho \frac{Y_{O_2}}{W_{O_2}} \exp\left(-\frac{19778}{T}\right)\right] T^{1/2} (\pi N)^{1/3} \left(\frac{6M}{\rho_s}\right)^{2/3}, \quad (11)$$

where N is the soot number density, and M is the soot mass density. T is the temperature of mixture gas, $Y_{C_2H_2}$ and Y_{O_2} and Y_{OH} are the species mass fraction of C_2H_2 , O_2 and OH respectively. $W_{C_2H_2}$ and W_{O_2} and W_{OH} are the molecular weight of C_2H_2 , O_2 and OH respectively. N_A is Avogadro's number ($6.022 \times 10^{26} \text{ kmol}^{-1}$). R is the universal gas constant, and ρ_s is the density of soot particles determined by Lindstedt [27], which has a value of $2000 \text{ kg} \cdot \text{m}^{-3}$. The coefficient values in each equations are $c_1=54 \text{ s}^{-1}$, $c_2=9000.6 \text{ kg} \cdot \text{m}(\text{kmol} \cdot \text{s})^{-1}$, $\eta = 0.13$, $c_3=105.81 \text{ kg} \cdot \text{m}(\text{kmol} \cdot \text{K}^{1/2} \cdot \text{s})^{-1}$, $c_4=8903.51 \text{ kg} \cdot \text{m}(\text{kmol} \cdot \text{K}^{1/2} \cdot \text{s})^{-1}$, respectively [26]. The source terms for soot number density S_N or soot mass density S_M can be expressed as follows.

$$S_N = \frac{1}{N_A} \left[\left(\frac{dN}{dt} \right)_{Inc.} + \left(\frac{dN}{dt} \right)_{Coa.} \right], \quad (12)$$

$$S_M = \frac{M_p}{N_A} \left(\frac{dN}{dt} \right)_{Inc.} + \left(\frac{dM}{dt} \right)_{Gro.} + \left(\frac{dM}{dt} \right)_{Oxi.}, \quad (13)$$

where M_p is the mass of a soot nucleus with a value of $1200 \text{ kg} \cdot \text{kmol}^{-1}$. Here, the assumption that the minimum number of carbon atoms is 100 is critical to create an incipient carbon particle.

The conservation equations for N and M are given as

$$\frac{\partial \rho \psi}{\partial t} + \frac{\partial \rho u_j \psi}{\partial x_j} = \frac{\partial}{\partial x_j} \left(\rho D_\psi \frac{\partial \psi}{\partial x_j} \right) + \gamma \frac{\mu}{T} \psi \frac{\partial T}{\partial x_j} + S_\psi, \quad (14)$$

where ψ represents N or M , and D_ψ is the diffusion coefficient of soot. The second term on the right-hand side of Eq. (14) expresses thermophoretic transport, where

$$\gamma = \frac{3}{4(1+\pi \cdot A/8)}, \quad (15)$$

and the accommodation coefficient A was set to 1.0.

The computational domain was 2D, and its size was $56 \text{ mm} \times 56 \text{ mm}$ for the conditions of equivalence ratios of 1.4, 1.6, and $36 \text{ mm} \times 36 \text{ mm}$ for the condition of the equivalence ratio of 1.8. Since the flame instability appeared at a large flame radius with the equivalence ratios of 1.4 and 1.6, the domain size was set larger under these conditions. A staggered mesh was adopted, and the number of grids was 700×700 points for equivalence ratios of 1.4 and 1.6, and 450×450 points for the equivalence ratio of 1.8. In all equivalence ratio cases, the grid size was 80 micrometers. Even in the case of smallest flame thickness of the equivalence ratio 1.4, this grid size is smaller than 1/10 of the flame thickness which was the recommended grid size proposed by Pitsch et al [15]. Here, the flame thickness was accounted for by Eq. (16) [22].

$$\delta_{th} = \frac{(T_b - T_u)}{\left| \frac{dT}{dx} \right|_{max}}, \quad (16)$$

where T_b and T_u shows burned gas temperature and unburned mixture temperature respectively. The $\left. \frac{dT}{dx} \right|_{max}$ denotes the maximum value of temperature gradient in the flame thickness.

Iso-octane was used as the fuel in this study, and the estimated Lewis numbers were 0.965, 0.953 and 0.941 at the equivalence ratio of 1.4, 1.6 and 1.8, respectively [5] [17] [29]. All values were smaller than unity. The initial temperature was 341 K, and the initial pressure was 0.10 MPa. To ignite the fuel, the initial flame kernel as the spark was given at the center of the domain, and the flame propagated outwardly from that initial flame kernel. The same initial flame kernel with a radius of 3 mm and temperature of 1807 K was given for all equivalence ratio conditions [19]. Sine waves with a wave number of 6 and amplitude of 0.3 mm were given for the flame front as the initial disturbance to reproduce the following flame instability as shown in Figure 1. The burning velocities of one-dimensional unstretched flames estimated by CHEMKIN [30] were 246, 101 and 59 mm/s at equivalence ratio of 1.4, 1.6 and 1.8, respectively. On the other hand, the burning velocities of the flames relative to the unburned mixture in this study were 405, 147 and 163mm/s at equivalence ratio 1.4, 1.6 and 1.8, respectively.

The discretization of the nonlinear terms of the momentum equation was derived from a second-order finite difference scheme, and the advection term of scalars was computed using the quadratic upstream interpolation for convective kinematics (QUICK) scheme. The third-order explicit Runge–Kutta method was used for time advancement. The boundary condition was set to a constant gradient.

The simulations were continued until the cellular structure was sufficiently developed. The termination time of the simulation was 10.5 msec at equivalence

ratio 1.4 and 16.5 msec at equivalence ratios of 1.6 and 1.8. The time step of the simulation was 5.0×10^{-7} s at equivalence ratios of 1.4 and 1.6 and, 2.5×10^{-7} s at an equivalence ratio of 1.8. The CPU times for the equivalence ratios of 1.4, 1.6, and 1.8 were 511 hours, 7,333 hours, and 10,707 hours, respectively, with Fujitsu PRIMERGY CX2550/CX2560 M4 of the Research Institute for Information Technology at Kyushu University.

3. Results and discussion

3.1. Flame shape

Figure 2 shows the instantaneous temperature distribution of the simulation results in all equivalence ratios. The non-dimensional Peclet number P_e was calculated using Eq. (17) from the flame radius r and preheat zone thickness δ_l of laminar flame given by Eq. (18) [29], where u_l is the unstretched laminar burning velocity calculated by CHEMKIN [30].

$$P_e = \frac{r}{\delta_l}, \quad (17)$$

$$\delta_l = \frac{\lambda_{th}}{c_p \rho u_l}. \quad (18)$$

The amplitude of the initial flame front disturbance gradually decreased, and the flame shape became smooth until the Peclet number reached critical values under any condition. After the Peclet number exceeded its critical value, the convex area plateaued. Subsequently, the flame front seemed to be a cellular structure. It was thought that these new cellular structures, which were not involved in the initial sine waves, demonstrated the flame instability. The Peclet number when the flame instability appeared on the flame front was smallest for the equivalence ratio of 1.8 among the three equivalence ratios.

Bradley et al. [13] [17] and Matalon et al. [11] proposed a theoretical approach for flame instability. The Lewis number was smaller than unity when the equivalence ratio was greater than 1.4, and it decreased with increasing the equivalence ratio [29]. These results imply that increasing the equivalence ratio of the iso-octane flame may advance the onset of the flame instability in the early stage of the flame propagation [13]. For a flame with a Lewis number smaller than unity, the burning velocity is increased in the convex area and, conversely,

decreases at the cusp area. These differences in the burning velocity may enhance the flame instability. According to the theoretical analysis of Bechtold and Matalon [12], depending on the Markstein number, a range of wavelengths of disturbance with upper and lower limits exists. The lower limit wave number decreases slightly with increasing Peclet number, but the upper limit wave number increases linearly with increasing Peclet number. As a result, this range of wavelengths of disturbance with upper and lower limits increases with decreasing Markstein number even if the flames have the same Peclet number.

In the results of the simulation shown in Figure 2, the range of unstable wave numbers seems to widen as the Peclet number increases because various sizes of perturbation appeared on the flames. The qualitative tendency of these results agrees with the theoretical approach. In addition, the range of unstable wave numbers also seems to widen as the Lewis number decreases, although flames could not be compared at the same Peclet number among the three equivalence ratios.

The equivalence ratio of 1.8 had the smallest Lewis number as shown in the previous section and the Peclet number of the onset of the cellular structures was smaller than those of the equivalence ratios of 1.4 and 1.6. The critical Peclet number is decreased as the Markstein number decreasing as shown by Bradley et al. [17].

Bradley et al. observed hydroxyl radicals (OH) within the spherically propagating, iso-octane, unstable flames at an equivalence ratio of 1.4 [13]. OH is one of the dominant chain carriers of combustion reactions. According to this observation of the cellular flame, the high concentration of OH was observed in

the convex area of the flame. On the other hand, the low concentration of OH was observed in the cusp area. Figure 3 shows the simulated results of the mass fraction distribution of OH in all equivalence ratios. OH was mainly formed locally at the regions of the convex area. This OH distribution showed a qualitative agreement with the observations of Bradley et al.

3.2. Flame stretch rate

The flame stretch rate is given by Eq. (19) [32],

$$\frac{1}{A} \frac{dA}{dt} = -\{\nabla \times (\vec{V}_{fluid} \times \vec{n})\} \cdot \vec{n} + (\vec{v} \cdot \vec{n})(\nabla \cdot \vec{n}), \quad (19)$$

where A is the area of the flame front, \vec{V}_{fluid} is the fluid velocity field, \vec{n} is a unit vector normal to the flame front, and \vec{v} is the displacement velocity of the flame front. The location of the flame front was defined as the grids where temperature was 1400 K. The flame stretch rate was calculated on this flame front although it is usually obtained at the cold boundary. The displacement velocity of the flame front was calculated under the assumption that the flame moved to the normal direction of flame front. The first term denotes the stretch due to the strain of the flow field across the flame front. The second term shows the stretch due to the displacement of the curved front [33].

Figure 4 shows the flame stretch rate and the flame radius at the location of each angular coordinate around the flame front at the timing of the onset of cellular structures. The flame stretch rate was sampled along the flame front every 2.5 deg. in the circumferential direction. While the convex area of the flame front has a positive value of the flame stretch rate, the concave area has a negative stretch rate at each equivalence ratio. In addition to the Darrieus-Landau hydrodynamic flame instability, the artificial initial disturbance was promoted by thermo-diffusive effects with the Lewis number smaller than unity. Subsequently, the local flame stretch rate varied depending on the local flame shape shown in Figure 2.

3.3. Temperature and soot formation distribution

Figure 5 shows the temperature distribution after the onset of the cellular structures along the radial direction at the convex and the cusp areas. The examined locations are shown in Figure 2. The pressure in the computational domain was increased by the adiabatic compression owing to the heat release so that the overall temperature of the simulation shown in Figure 5 exceeds the adiabatic flame temperature at the initial pressure. The convex area shown in Figure 5 has a small positive stretch rate, on the other hand, the cusp area has a negative stretch rate. Both the temperature and the temperature gradient at the cusp area with the negative flame stretch rate were lower than those at the convex area with the positive flame stretch rate.

The balance between the molecular diffusion of the deficient component of the mixture and the heat conduction in the unstretched flame is shifted by the flame stretch [10]. Owing to the thermo-diffusive effects of the mixture with Lewis number smaller than unity [10-15] [17], the flame temperature and consequently the burning velocity increased at the convex flame front area with the positive flame stretch rate and decreased at the cusp area with the negative flame stretch rate. As for the variation of the flame temperature with the equivalence ratio, the difference in temperature between the positive and the negative flame stretch rate areas was increased as with the increase in the equivalence ratio.

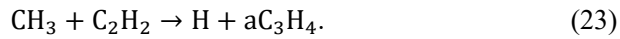
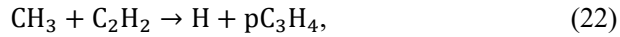
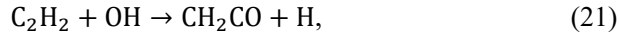
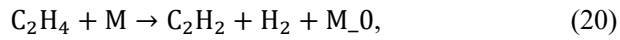
Figure 6 shows the distribution of the soot volume fractions ($= M / \rho_s$). In all equivalence ratio conditions, the soot distributed behind the flame front. Especially, the soot volume fraction was high behind the cusp area. This soot distribution agreed with the experimental observation of the luminous flame due

to the soot radiation [5].

The soot formation was dominated by four processes of soot inception, surface growth, coagulation, and oxidation [34] [35]. The rate of change in M ($= dM / dt$) through each process was modeled by Eqs. (8–11) and (14). Equation (8) yielded the inception rate and this was transformed to M using the first term of Eq. (13) [6] [26] [36] [37]. Figure 7 shows the soot volume fraction and the rates of volume fraction for each process ($= dM / dt / \rho_s$) at the time flame of instability appeared. The examined locations are same in Figure 5. The soot volume fraction was the highest at the equivalence ratio of 1.8 for all the conditions. The rate of coagulation is not shown herein because the coagulation does not contribute to the volume fraction.

However, the rates of volume fraction by each process were different when the positive and the negative flame stretch rate areas were compared; the rate of surface growth at the negative flame stretch rate area was higher than that at the positive flame stretch rate area. The rate of oxidation was proportional to the soot mass fraction, and therefore the difference in the soot volume fraction may mainly be due to the rate of surface growth. As the equivalence ratio increased, the rate of surface growth also contributed significantly to the soot volume fraction. It is well-known that an inception rate of soot primary particles has significant correlation to C_2H_2 concentration in a saturated hydrocarbon flame [39] and the simplified inception model like Leung et al. [38] has been confirmed that it is able to capture the qualitative trend of the soot formation in n-decane flames [40]. However, it should be noted that the characteristics of the inception might be affected by the difference in the location where the peak value of the precursor species appears [41], while it is unlikely to occur due to that the flame thickness

is too thin in this study. Thus, Eqs. (8) and (9) could provide an appropriate prediction for soot inception and surface growth formation. C_2H_2 contributes to increasing the rate of inception and surface growth through a specific reaction mechanism [34] [35]. Figure 8 shows the mass fraction of C_2H_2 at the same point in time as Figure 5 and Figure 7. The C_2H_2 distribution was similar to the distribution of the soot volume fraction shown in Figure 6. Equations (20–23) show the major reactions of C_2H_2 formation and consumption whose reactant distribution was similar to the C_2H_2 distribution. Equation (20) shows the formation reaction of C_2H_2 , whereas Eqs. (21–23) show the consumption reactions. As shown in Eq. (20), C_2H_2 was formed from C_2H_4 in the reaction pathway of iso-octane [43] [44]. The reactant distributions involved in Eq. (20) are shown in Figure 8.



Here, M_0 denotes the third body. Figure 9 shows the reaction rates defined as Eqs. (20–23) comparing the positive and the negative flame stretch rate areas at the equivalence ratio of 1.8 which has the largest soot volume fraction in all equivalence ratios. The reaction rate of C_2H_2 formation from C_2H_4 was superior to the reaction rate of C_2H_2 consumption, and the reaction rate of C_2H_2 at the negative flame stretch rate area behind the flame front was higher than that in the positive flame stretch rate area. These differences were caused by the low temperature and the temperature gradient due to the thermo-diffusive effects.

Considering the results of Fig. 7, the rate of surface growth was more sensitive to

increasing C_2H_2 in the negative flame stretch rate area than the rate of inception. Thus, the rate of surface growth at the negative flame stretch rate area was higher than that at the positive flame stretch rate area, and the soot volume fraction at the negative flame stretch rate area was larger than that at the positive flame stretch rate area. In addition, because of the high concentration of C_2H_2 at the negative flame stretch rate area behind the flame front, the soot might be distributed as shown in Figure 6. Owing to the low temperature and the temperature gradient at the negative flame stretch rate area, the oxidation of the soot might not be enhanced compared to the positive flame stretch rate area. As a result, the soot remained behind the flame front in the cusp area whose the flame stretch rate was negative, and the luminous flame due to the soot radiation might be observed behind the flame front, similar to the experimental observation results [5].

As for the variation of the soot formation with the equivalence ratio, the Peclet number of the onset of cellular structure on the flame front at the equivalence ratio of 1.8 was the smaller than those of at the equivalence ratios of 1.4 and 1.6, as mentioned in Section 3.1. The differences in temperature between the positive and the negative flame stretch rate areas appeared in the early stage of the flame propagation. This might have affected the soot formation at the negative flame stretch rate area from the early stage of the flame propagation. The soot formation at the early stage induced the higher soot volume fraction behind the flame front at the equivalence ratio of 1.8 when compared with the other equivalence ratios.

4. Conclusions

Soot formation in outwardly propagating iso-octane rich unstable cellular flames was investigated by means of a two-dimensional numerical simulation at equivalence ratios of 1.4, 1.6, and 1.8.

In the unstable cellular flames, there was a positive stretch rate at the convex area of the flame front; conversely, there was a negative stretch rate at the cusp area towards the unburned mixture. Both the temperature and the temperature gradient at the negative flame stretch rate area were lower than those at the positive flame stretch rate area.

It was also observed that the soot formation at the negative flame stretch rate area was higher than that at the positive flame stretch rate area, and the soot formation was dominated by the surface growth. The rate of surface growth was affected by C_2H_2 generation, and C_2H_2 was generated by C_2H_4 decomposition. The reaction rate of the C_2H_2 formation from C_2H_4 at the negative flame stretch rate area was higher than that at the positive flame stretch rate area. This was caused by the low temperature and the temperature gradient due to the thermo-diffusive effects at the negative flame stretch rate area.

It became clear that the difference in the soot distribution was caused by the differences in the temperature and the C_2H_2 distribution, which were originated from the difference in the flame stretch rate and the thermo-diffusive effects of the unstable flame with the Lewis number smaller than unity.

Acknowledgments

This work was supported by JSPS KAKENHI Grant Number JP19H02080.

References

- [1] Abata D, Evans RL. Automotive Engine Alternatives. Plenum Publishing Corporation New York 1987.
- [2] Yan-zhao A, Sheng-ping T, Yi-qiang P, Jing Q, Xiang L, Hua Z. An experimental study of polycyclic aromatic hydrocarbons and soot emissions from a GDI engine fueled with commercial gasoline. *Fuel* 2016;164:160-171.
- [3] Johansen LCR, Hemdal S. In cylinder visualization of stratified combustion of E85 and main sources of soot formation. *Fuel* 2015;159:392-411.
- [4] Lemaire R, Boudreau A, Seers P. Performance and emissions of a DISI engine fueled with gasoline/ethanol and gasoline/C-4 oxygenate blends – Development of a PM index correlation for particulate matter emission assessment. *Fuel* 2019;241:1172-1183.
- [5] Miyata K, Kitagawa T, Nagano Y, Fujisaki Y. Observation of Particulate Matter in iso-Octane/Air Premixed Flames with Transmission Electron Microscope. *Proc Annu Conf Jpn Inst Energy* 2015;188 (in Japanese).
- [6] Watanabe H, Kurose R, Komori S, Pitsch H. Effect of radiation on spray flame characteristics and soot formation. *Combust Flame* 2008;152:2-13.
- [7] Hayashi J, Watanabe H, Kurose R, Akamatsu F. Effects of fuel droplet size on soot formation in spray flames formed in a laminar counterflow. *Combust Flame* 2011;158:2559-2568.
- [8] Hayashi J, Hashimoto N, Nakatsuka N, Tainaka K, Tsuji H, Tanno K, Watanabe H, Makino H, Akamatsu F. Simultaneous imaging of Mie

- scattering, PAHs laser induced fluorescence and soot laser induced incandescence to a lab-scale turbulent jet pulverized coal flame. *Proc Combust Inst* 2019;37:3045-3052.
- [9] Brookes SJ, Moss JB. Predictions of soot and thermal radiation properties in confined turbulent jet diffusion flames. *Combust Flame* 1999;116:486-503.
- [10] Williams FA. *Combustion Theory* Second Edition. 2018
- [11] Bechtold JK, Matalon M. Hydrodynamic and diffusion effects on the stability of spherically expanding flames. *Combust Flame* 1987;67:77-90.
- [12] Bechtold JK, Matalon M. The dependence of the Markstein length on stoichiometry. *Combust Flame* 2001;127:1906-1913.
- [13] Bradley D, Sheppard CGW, Woolley R, Greenhalgh DA, Lockett RD. The development and structure of flame instabilities and cellularity at low Markstein numbers in explosions. *Combust Flame* 2000;122:195-209.
- [14] Addabbo R, Bechtold JK, Matalon M. Wrinkling of Spherically Expanding Flames. *Proc Combust Inst* 2002;29:1527-1535.
- [15] Berger L, Kleinheinz K, Attili A, Pitsch H. Characteristic Patterns of Thermodiffusively Unstable Premixed Lean Hydrogen Flames. *Proc Combust Inst* 2019;37:1879-1886.
- [16] Sharpe GJ, Falle SARG. Numerical simulations of premixed flame cellular instability for a simple chain-branching model. *Combust Flame* 2011;158:925-934.
- [17] Bradley D, Harper CM. The development of instabilities in laminar explosion flames. *Combust Flame* 1994;99:562-572.
- [18] Bradley D, Hicks RA, Lawes M, Sheppard CG, Woolley R. The

- measurement of laminar burning velocities and Markstein numbers for iso-octane-air and iso-octane-n-heptane-air mixtures at elevated temperatures and pressures in an explosion bomb. *Combust Flame* 1998;115:126-144.
- [19] Kadowaki S, Takahashi H, Kobayashi H. The Effects of Radiation on the Dynamic Behavior of Cellular Premixed Flames Generated by Intrinsic Instability. *Proc Combust Inst* 2011;33:1:1153-116.
- [20] Kurose R(2021). http://www.tse.me.kyoto-u.ac.jp/members/kurose/link_e.php
- [21] Shehab H, Watanabe H, Kurose R, Kitagawa T. Numerical study on the effects of turbulence scale on spherically propagating hydrogen flames within multiple flame radii. *Int. J. Automotive Eng.* 2019;10:4:292-298.
- [22] Shehab H. Morphology, Structure and Burning Velocities of Spherically Propagating Premixed Turbulent Hydrogen Flames. A Doctoral Diss 2020.
- [23] Poinot T, Veynante D. Theoretical and Numerical Combustion. Second Edition. Philadelphia: R.T. Edwards 2005.
- [24] Giovangigli V. Convergent iterative methods for multicomponent diffusion. *IMPACT Comput. Sci. Eng.* 1991;3:3:244–276.
- [25] Blanquart G, Pepiot P, Pitsch H. Chemical mechanism for high temperature combustion of engine relevant fuels with emphasis on soot precursors. *Combust Flame* 2009;156:588–607
- [26] Watanabe H, Kurose R, Hayashi M, Kitano T, Komori S. Effect of ambient pressure and precursors on soot formation. *Adv Powder Tech* 2014;25.
- [27] Lindstedt PR. Simplified soot nucleation and surface growth steps for non-premixed flames, in: *Soot Formation in Combustion. Springer Series in*

Chem Phys Berlin 1994;417-441

- [28] Cai L, Pitsch H. Optimized chemical mechanism for combustion of gasoline surrogate fuels. *Combust Flame* 2015;162:1623-1637.
- [29] Kitagawa T, Maruyama K, Nakahara T, Kado K, Hayakawa A. Effect of Pressure on Laminar and Turbulent Burning Velocities of Iso-octane Premixed Flames. *Transactions of JSAE* 2009;20094051 (in Japanese).
- [30] CHEMKIN-Pro 2021R1, ANSYS, Inc., San Diego, 2021.
- [31] Kitagawa T, Togami Y, Harada K, Ogawa T. Effects of Pressure on Unstretched Laminar Burning Velocity, Markstein Length and Cellularity of Propagating Spherical Laminar Flames. *Trans Jpn. Soc Mech Eng Series B* 2004;70:696:2197-2204 (in Japanese).
- [32] Ishizuka S. Flame Stretch and Statistical Characteristics of Steady Flames. J-GLOBAL ID:200909096106443887 1999;116:49-70 (in Japanese).
- [33] Matalon M. On Flame Stretch. *Combust Sci Tech* 1983;31:169-181.
- [34] Hashimoto J, Ishii K, Akihama K. A Soot Formation Model for Gasoline Surrogate Fuel Applying the Sectional Method to PAH Growth. *Transactions of JSAE* 2019;20194902 (in Japanese).
- [35] Akihama K, Kadowaki N, Imamura O, Ishii K, Hashimoto J. Study on Soot Formation Model for Gasoline Surrogate Fuel (Second Report). *Transactions of JSAE* 2019;20194671 (in Japanese).
- [36] Yan-zhao A, Xiang L, Sheng-ping T, Kun W, Yi-qiang P, Jing Q, Hua Z. Development of a soot particle model with PAHs as precursors through simulations and experiments. *Fuel* 2016;179:246-257.
- [37] Feiyang Z, Wenbin Y, Wanhua S. Sensitivity study of engine soot forming

- using detailed soot modeling oriented in soot surface growth dynamic. *Fuel* 2016;168:81-90.
- [38] Leung KM, Lindstedt RP, and Jones WP. A simplified reaction mechanism for soot formation in nonpremixed flames. *Combust Flame* 1991;87:289-305.
- [39] Frenklach M, Clary DW, William C, Gardiner J, Stein SE. Detailed kinetic Modeling of Soot Formation in Shock-tube Pyrolysis of Acetylene. 20th Symp Combust 1984;887-901.
- [40] Watanabe H, Kurose R, Komori S, Pitsch H. Effects of radiation on spray flame characteristics and soot formation. *Combust Flame* 2018;152:2-13.
- [41] Watanabe H, Kurose R, Hayashi M, Kitano T, Komori S, Effects of ambient pressure and precursors on soot formation in spray flame. *Adv Powder Tech* 2014;25:1376-1387.
- [42] Kholghy M R, Veshkini A, Thomson M J. The core-shell internal nanostructure of soot - A criterion to model soot maturity. *Carbon* 2016;100:508-536.
- [43] Davis SG, Law CK. Laminar Flame Speed and Oxidation Kinetics of iso-Octane-Air and n-Heptane-air Flames, 27th Symp Combust 1998;521-527.
- [44] Pitsch H, Peters N, Seshadri K. Numerical and Asymptotic Studies of the Structure of Premixed Iso-octane Flames. 26th Symp Combust 1996;763-771.

Figure List

Figure 1. Temperature profile of initial flame kernel in this simulation.

Figure 2. Instantaneous temperature distribution organized by equivalence ratio.

Figure 3. Instantaneous OH distribution organized by equivalence ratio.

Figure 4. Flame stretch rate and flame radius organized by equivalence ratio.

Figure 5. Comparison of temperature distribution between convex and cusp area of unstable flames.

Figure 6. Development of soot volume fraction distribution for three equivalence ratios.

Figure 7. Contribution of each soot formation process.

Figure 8. C_2H_2 and reaction products affecting C_2H_2 generation.

Figure 9. Reaction rates of formation/consumption reactions of C_2H_2 at $\Phi=1.8$ and Peclet number = 35.

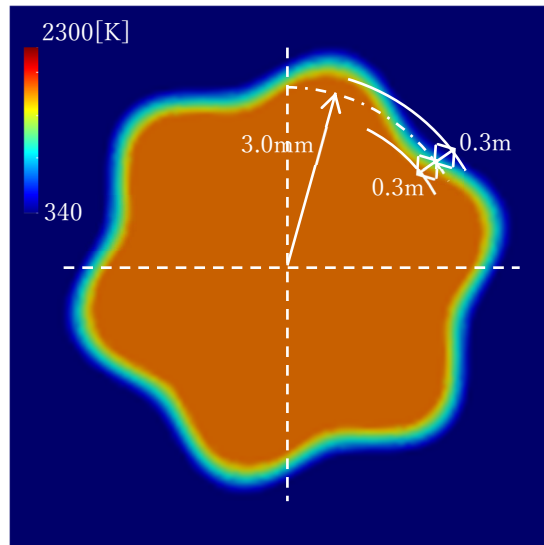


Figure 1. Temperature profile of initial flame kernel in this simulation.

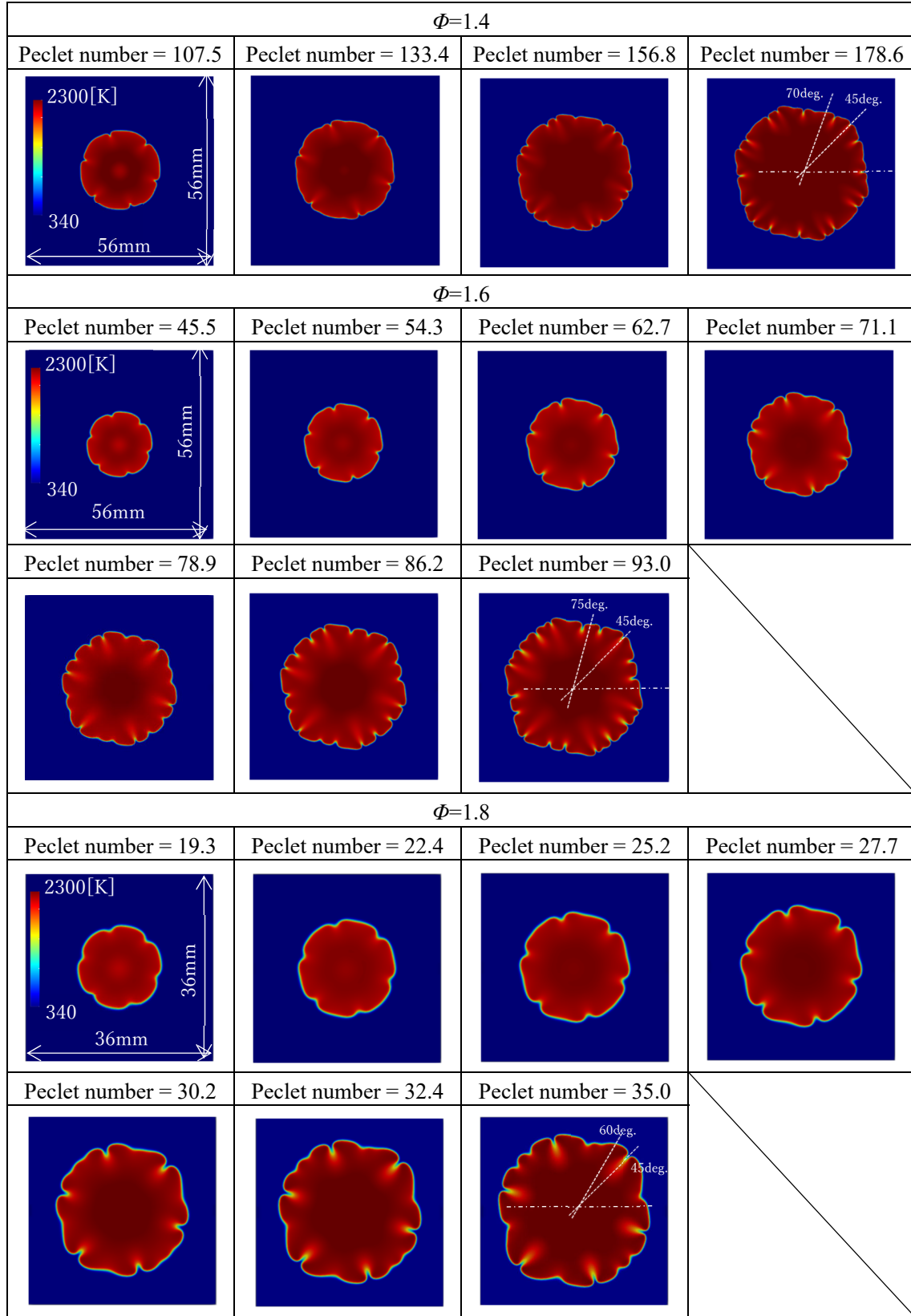


Figure 2. Instantaneous temperature distribution organized by equivalence ratio.

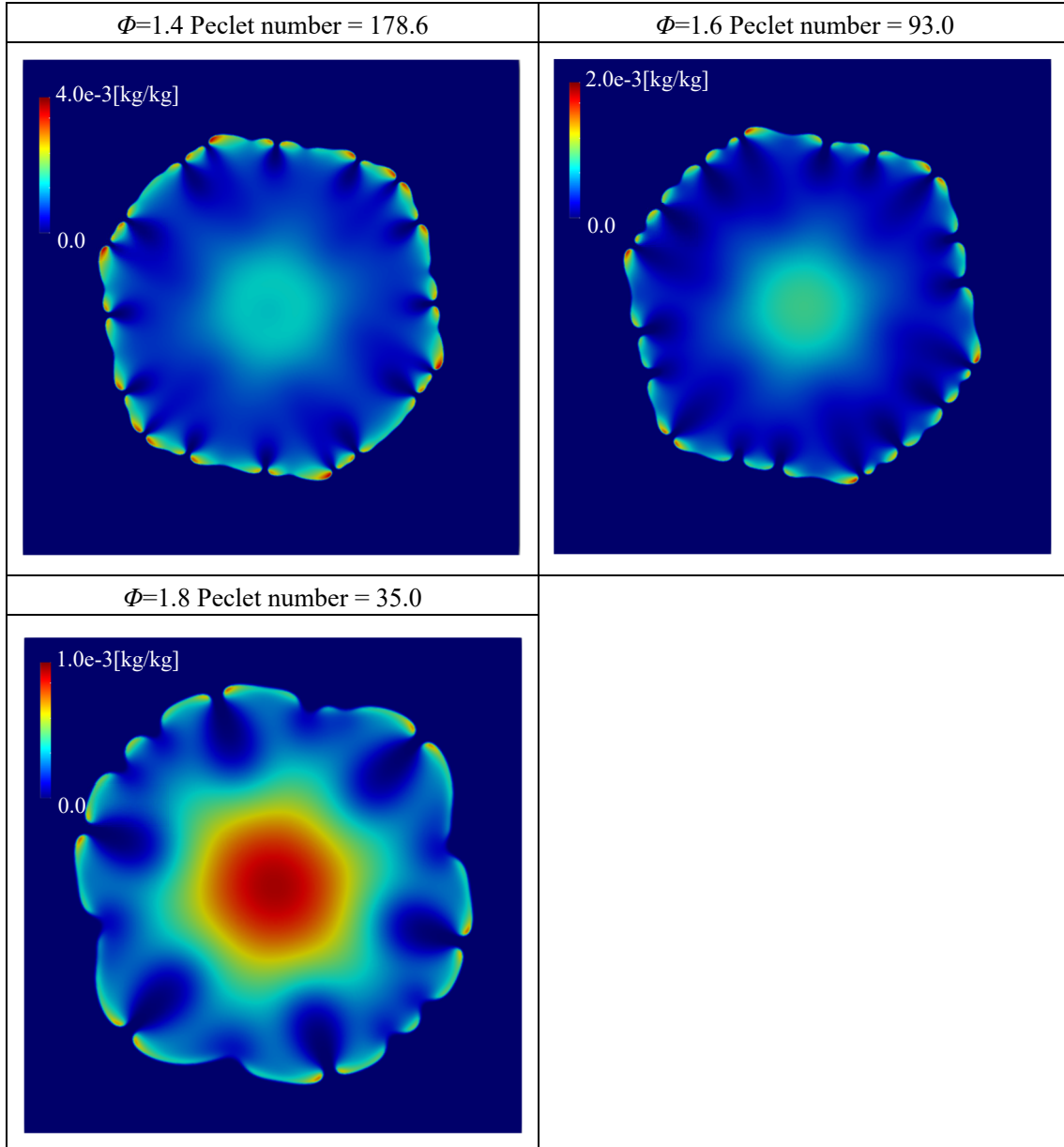


Figure 3. Instantaneous OH distribution organized by equivalence ratio.

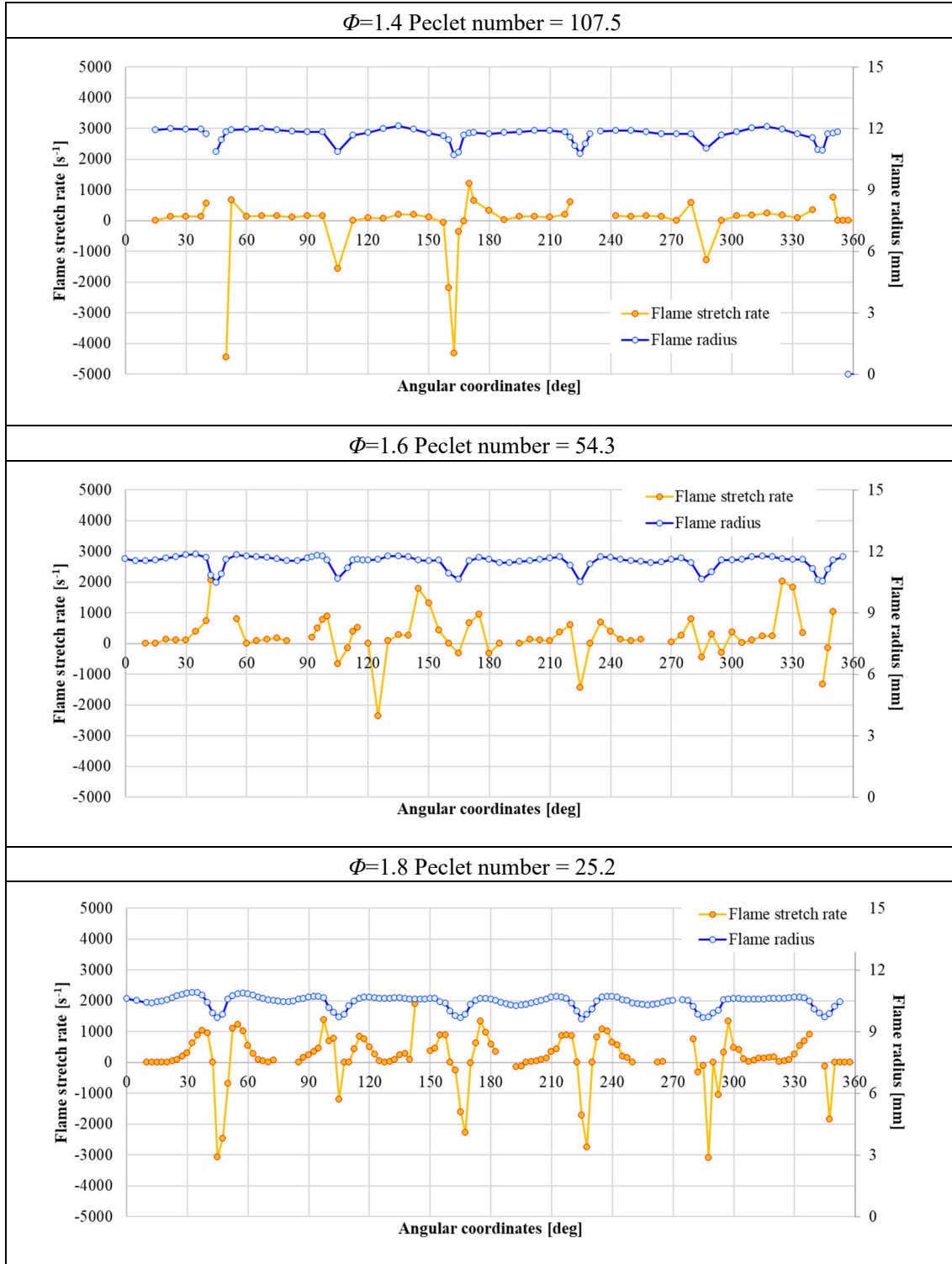


Figure 4. Flame stretch rate and flame radius organized by equivalence ratio.

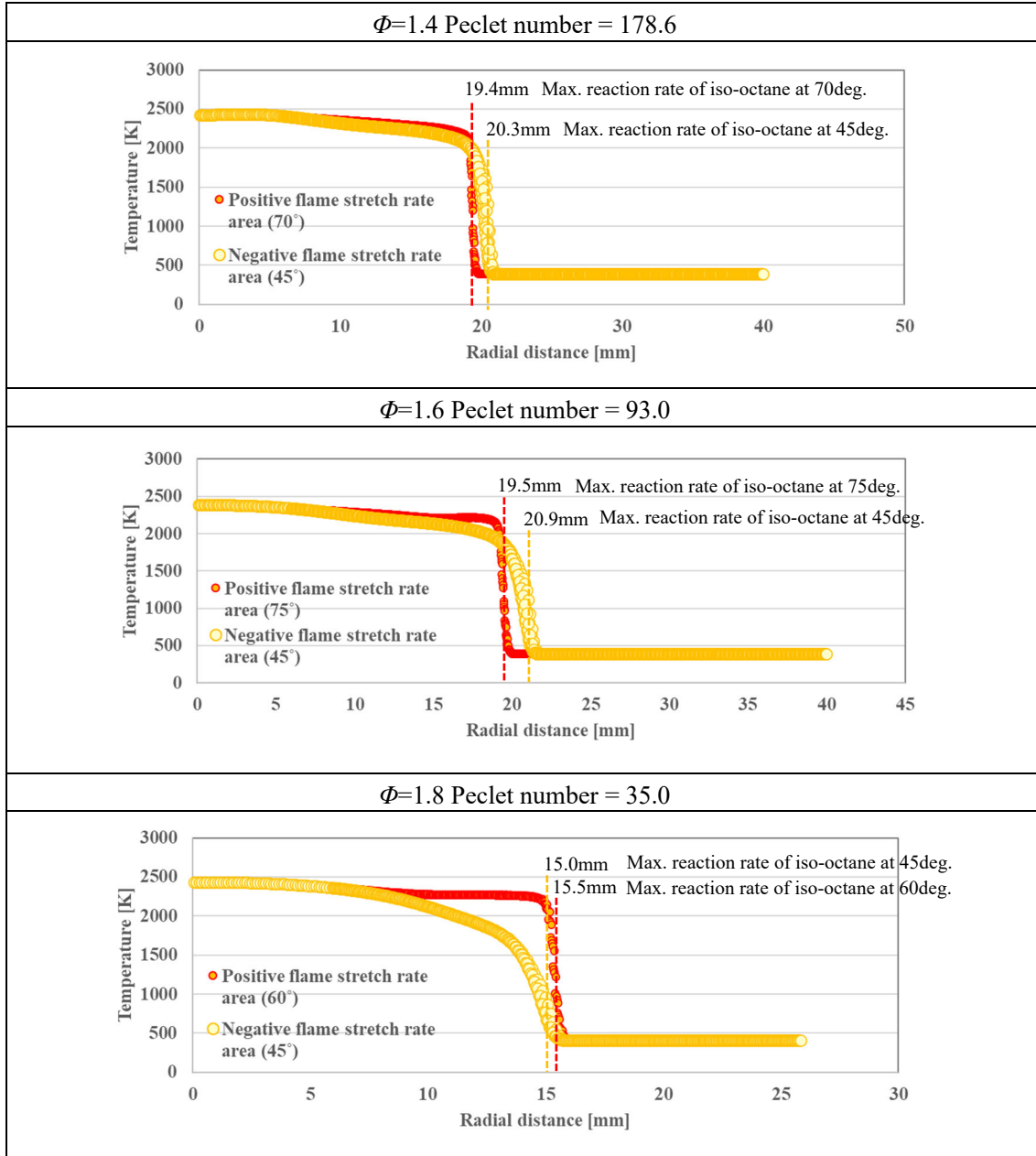


Figure 5. Comparison of temperature distribution between convex and cusp area of unstable flames.

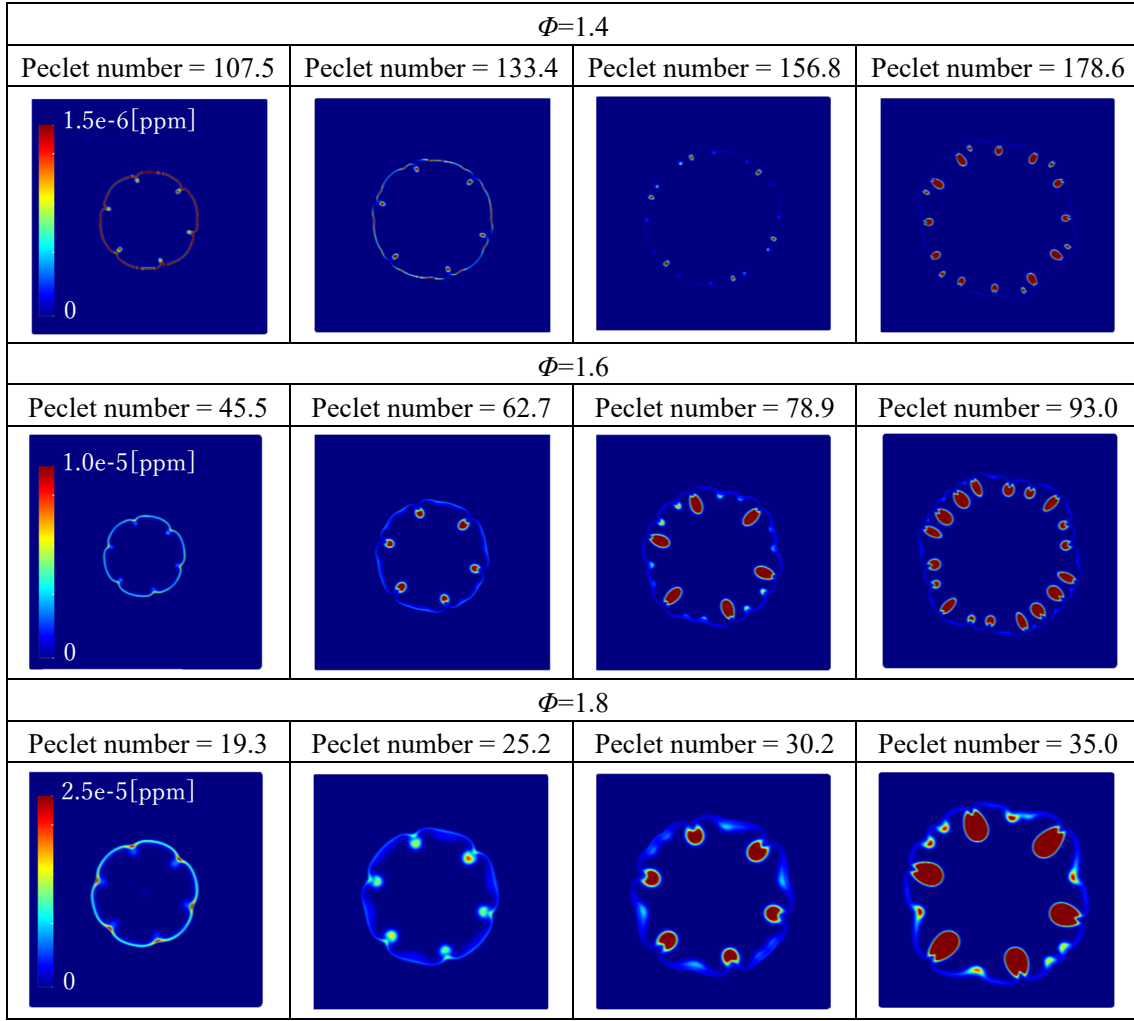


Figure 6. Development of soot volume fraction distribution for three equivalence ratios.

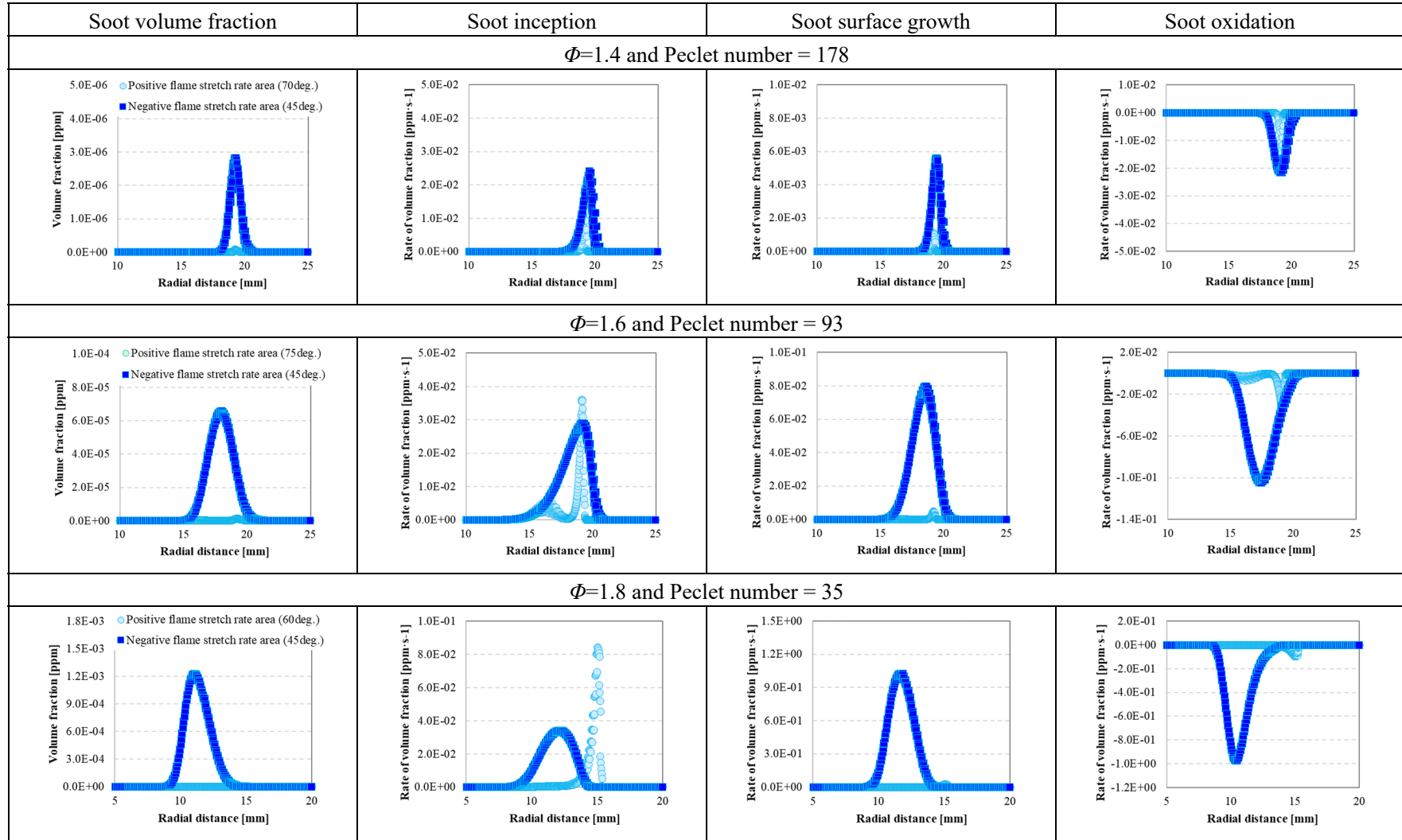


Figure 7. Contribution of each soot formation process.

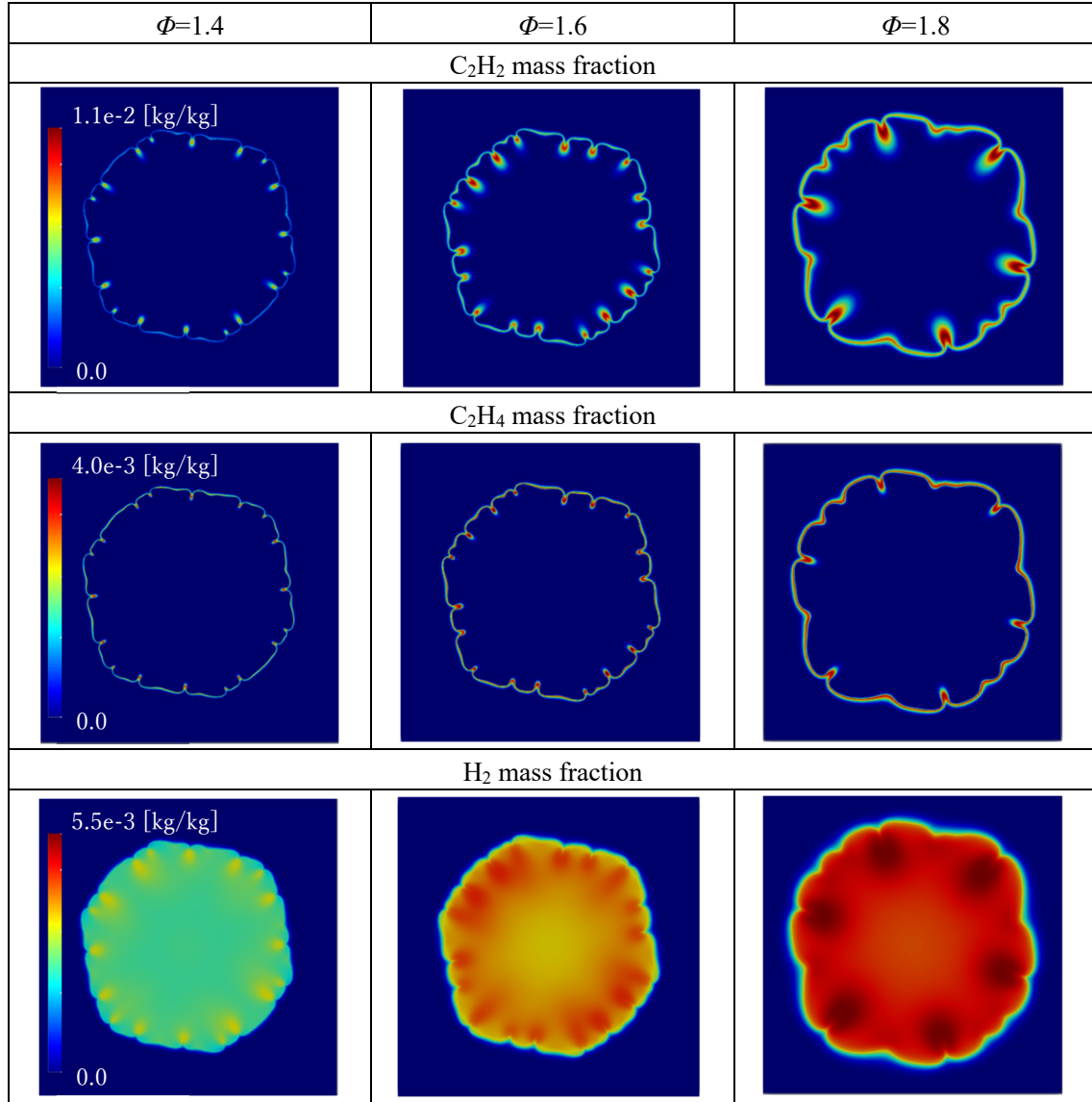


Figure 8. C₂H₂ and reaction products affecting C₂H₂ generation.

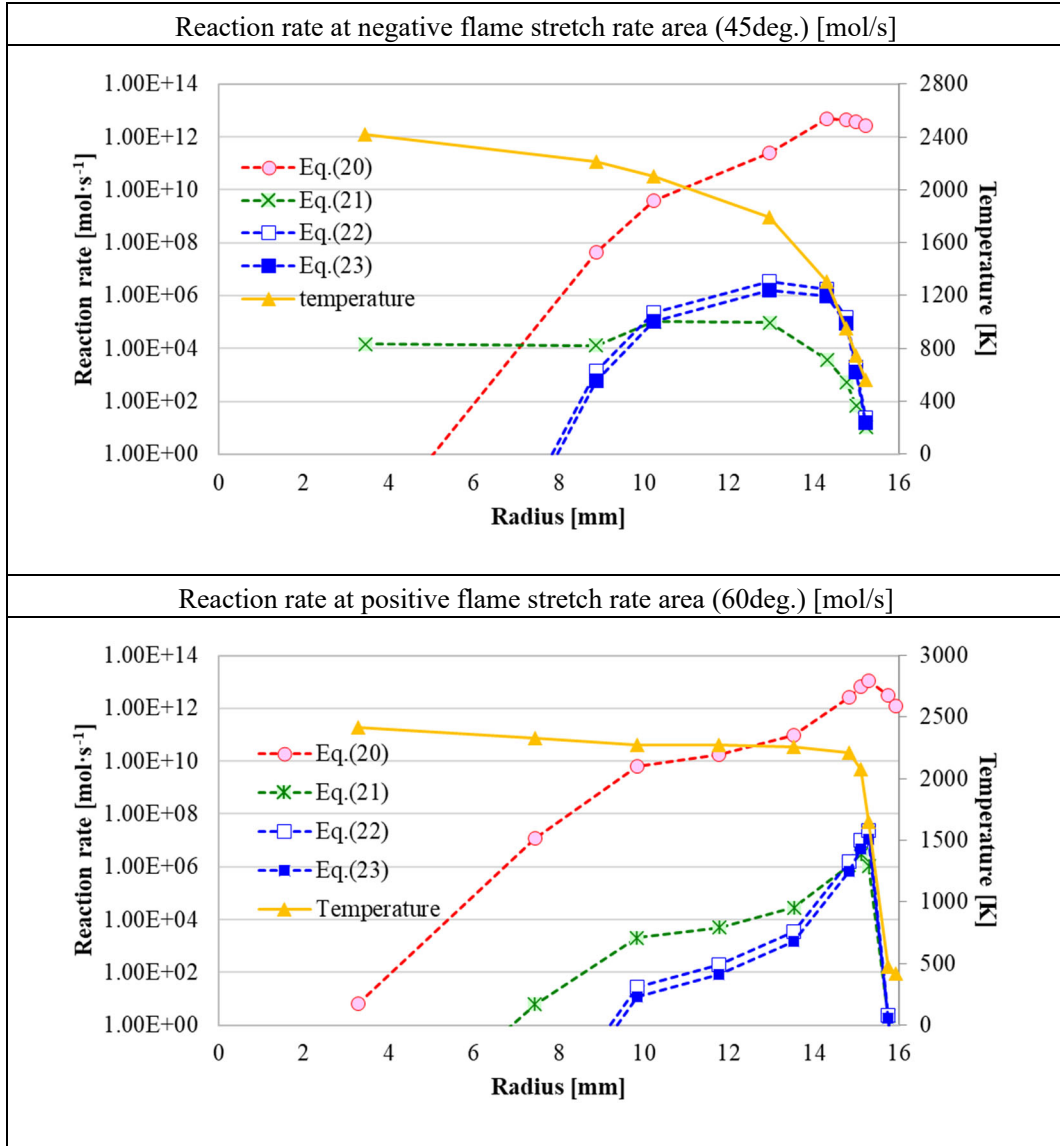


Figure 9. Reaction rates of formation/consumption reactions of C₂H₂ at $\Phi=1.8$ and Peclet number =

35.